XL CILAMCE
IBERO-LATIN AMERICAN CONGRESS ON COMPUTATIONAL METHODS IN ENGINEERING
NOVEMBER 11-14, 2019
Praiamar Natal Hotel & Convention Natal, RN-BRAZIL

GEOMETRICALLY NONLINEAR LIMIT POINT ANALYSIS OF CONCRETE STRUCTURES WITH DAMAGE AND TEMPERATURE EFFECTS

Henrique C. F. Curci
Eduardo M. B. Campello
Henrique C. Gomes
henrique.curci@usp.br
campello@usp.br
henrique.campelo@usp.br

Flávio L. Maranhão
flavio.maranhao@usp.br
Department of Civil Engineering Construction, University of São Paulo
Av. Prof. Almeida Prado, trav.2 nº. 83, 05508-070, São Paulo/SP, Brazil

Abstract. This work seeks to analyse a buckling and limit point problems of concrete structures based on a geometrically nonlinear formulation with the consideration of thermal effects and material damage. The thermal expansion effects due to heating processes in confined structures have an important role in the stress-strain evolution. Damage is treated in a simple way through the Mazar's continuum damage model. The resulting equations are approached by means of a finite element discretization, the solution of which is pursued through an incremental, iterative standard Newton-Raphson numerical scheme implemented by the authors in an in-house nonlinear FEM code. We then present two examples of numerical simulations to validate our formulation and illustrate its applicability to the nonlinear stability analysis of slender concrete structures under thermal loads.

Keywords: Stability analysis, geometrical nonlinearities, damage, thermal effects, concrete structures

1 Introduction

The evolution of design methods and construction techniques over the last decades allowed several advances in concrete structures that resulted in cost reduction and the design of more efficient structures. The quest for lighter solutions and new constructive methods have promoted the increase of slenderer constructions, invariably including (but not restricted to) composite steel-concrete beams and columns, prestressed concrete elements, thinner slabs, shallow arches and concrete shells. From the structural point of view, the design of slender structures typically requires careful verification of global/local instabilities, second order effects and vibration analysis under service loads. This brings into consideration the determination of the structure´s critical loads, in order to evaluate buckling phenomena and limit point ultimate strength such to allow for their comparison to the external solicitations. Due to both geometric and material effects, reliable computation of critical loads usually requires a nonlinear analysis, even if post-critical behavior is not of interest. Compressive stresses originated from the external loadings and imposed deformations (e.g. due to temperature changes and moisture increase in structures subjected to axial confinement) are the primary sources of critical behavior for slender parts. Figure 1-a shows a reinforced concrete shear wall (from Elwood [1]) after failure due to vertical compressive stresses as triggered by an earthquake.

A number of studies take into consideration nonlinear global instabilities in slender beams and shallow arches due to thermal loadings [2-3], in reinforced concrete columns under fire conditions [4] and in encased composite (steel-concrete) columns [5], to name and cite just a few. One interesting example of global instability in slender concrete elements can be observed in road slabs and bridge decks directly exposed to environmental loads, wherein thermally-induced expansion may trigger buckling and limit point instability (see Fig. 1-b). This phenomenon is commonly known as “blow-up buckling” and one of its causes is the restriction to horizontal movement of the concrete slab with insufficient (or even the complete absence of) expansion joints. Kerr et al. [6] and Yang et al. [7] studied with an analytical formulation the buckling response of such elements to several temperatures, geometrical and mechanical situations, trying to obtain a safe-temperature zone to avoid the instability failure.

Figure 1. a – Rupture and spalling of V-shaped RC shear wall (extracted from [1]). b- Road pavement “blow-up buckling” due to thermal expansion effect.

From the micromechanics point of view, the concrete matrix is well known for its stochastic behavior and dependence of various (both material and mechanical) properties. As a heterogeneous brittle material, one also expects the possibility of failure due to the initiation of micro-cracks followed by their progressive spreading along the critically stressed regions, often well before the appearance of such deformations that characterizes global buckling and post-buckling states. Accounting for the

evolution of damage through those areas is thereby critically important. Therefrom, the material response becomes nonlinear and the instability turns to be dependent on the effective area that resists those stresses, such that the phenomenon is transformed into a limit point problem, in the vicinity of which any increment in external loads cannot be appropriately balanced by the structural element´s deformation, eventually leading to a global-local failure (and constituting an ultimate limit state for design).

This work presents a geometrically nonlinear formulation for the analysis of buckling and limit point problems of concrete structures with consideration of thermal effects and material damage. Damage is treated in a simple way through the Mazar's continuum damage model. The resulting equations are approached by means of a finite element discretization, the solution of which is pursued through an incremental, iterative Newton-Raphson numerical scheme implemented by the authors in an in-house nonlinear FEM code. We then present examples of numerical simulations to validate our formulation and illustrate its applicability to the nonlinear stability analysis of slender concrete structures under thermal loads. The paper is organized as follows. In section 2 we present our formulation and its corresponding numerical solution scheme. In section 3 we present our numerical examples, including a brief discussion on the results. In section 4 we close the paper with our conclusions and final considerations. Throughout the text, plain italic letters ($a,b,\mathrm{K}\,,a\,,b,\mathrm{K}\,,A,B,\mathrm{K}$) denote scalar quantities; boldface lowercase italic letters ($\boldsymbol{a},\boldsymbol{b},\mathrm{K}\,,\boldsymbol{a}\,,\boldsymbol{b},\mathrm{K}$) denote vectors; and boldface capital italic letters ($\boldsymbol{A},\boldsymbol{B},\ldots$) denote second-order tensors in a three-dimensional Euclidean space. The inner product of two vectors is denoted by $\boldsymbol{u}\times\boldsymbol{v}$, and the norm of a vector by $\|\boldsymbol{u}\| = \sqrt{\boldsymbol{u}\times\boldsymbol{u}}$.

2 Formulation and numerical solution scheme

We restrict ourselves to two-dimensional problems here (plane-strain or plane-stress). We follow a total Lagrangian kinematical description for arbitrarily large deformations, into which we subsequently introduce our constitutive representation. For this latter, we assume a special type of (hyperelastic) neo-Hookean material for the elastic domain, the so-called Simo-Ciarlet material (see Campello [8]-[9] and Gomes [8]), and then we introduce temperature-induced deformations and damage (via a Marzar´s model) in a simple yet fully consistent way.

2.1 Kinematics and equilibrium

The kinematic formulation presented in this section is geometrically exact and considers the solid´s deformation in a two-dimensional setting (plane-strain or plane-stress conditions). Let a body be described by its inner region Ω, contour Γ, position vectors $\boldsymbol{x}^r$ (in the reference configuration) and $\boldsymbol{x}$ (in the current configuration), and be subjected to a displacement field $\boldsymbol{u}$, as shown in Fig. 2. Notation with a superscripted "r" (as in $\blacksquare^r$) is adopted throughout to designate quantities in the reference configuration, whereas notation with an upper bar ($\bar{\blacksquare}$) indicates prescribed values (e.g. for tractions $\bar{\boldsymbol{t}}$ and displacements $\bar{\boldsymbol{u}}$ at the solid´s boundaries).

The total deformation gradient $\boldsymbol{F}_T$ is given by the derivative of the current material points´ positions (i.e., at the deformed configuration) with respect to the corresponding positions at the reference configuration. This can be written as

$$\boldsymbol{F}_T = \nabla\boldsymbol{x} = \frac{\partial\boldsymbol{x}}{\partial\boldsymbol{x}^r} = \boldsymbol{f}_{Ti}\otimes\boldsymbol{e}_i = [\boldsymbol{f}_{T1}\,\boldsymbol{f}_{T2}\;\;\boldsymbol{e}_3]\,, \tag{1}$$

where $\boldsymbol{e}_i$ is the global (orthonormal) reference base and $\boldsymbol{f}_{Ti}$ are the column-vectors of $\boldsymbol{F}_T$. Likewise, the total displacement gradient $\boldsymbol{L}_T$ can be expressed in terms of its column-vectors $\boldsymbol{\gamma}_{Ti}$ as follows

$$\boldsymbol{L}_T = \nabla\boldsymbol{u} = \frac{\partial\boldsymbol{u}}{\partial\boldsymbol{x}^r} = \boldsymbol{\gamma}_{Ti}\otimes\boldsymbol{e}_i = [\boldsymbol{\gamma}_{T1}\,\boldsymbol{\gamma}_{T2}\,\boldsymbol{0}]. \tag{2}$$

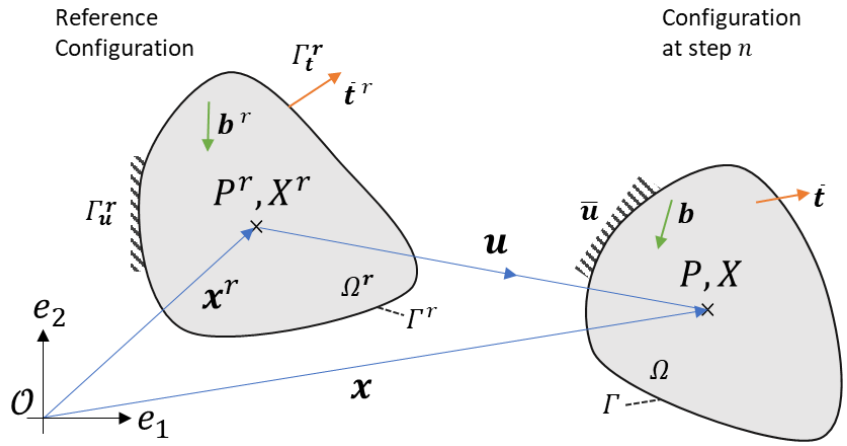

Figure 2. Deformable solid under arbitrary (nonlinear) transformation.

Note that $\boldsymbol{F}_T$ and $\boldsymbol{L}_T$ are already written with the plane-strain particulatization, in which both $\boldsymbol{f}_{T3} = \boldsymbol{e}_3$ and $\boldsymbol{\gamma}_{T3} = \boldsymbol{0}$ are considered. In order to account for thermal and damage effects in a fully consistent way for arbitrarily large deformations, we use the concept of intermediate (fictitious) natural configurations, similarly as done for finite-strain elastoplasticity (see, e.g., Campello [8] and Campello et al. [11]). Accordingly, the total deformation gradient is written through a multiplicative decomposition as a function of the intermediate deformation gradients $\boldsymbol{F}_\theta$ (relative to the thermal deformation) and $\boldsymbol{F}_e$ (relative to the elastic deformation) (see also Fig. 3):

$$\mathbf{F}_\mathrm{T} = \mathbf{F}_\mathrm{e}.\mathbf{F}_\theta, \quad \textit{with} \quad \mathbf{F}_\mathrm{e} = \mathbf{f}_{\mathrm{ei}} \otimes \mathbf{e}_\mathrm{i}. \tag{3}$$

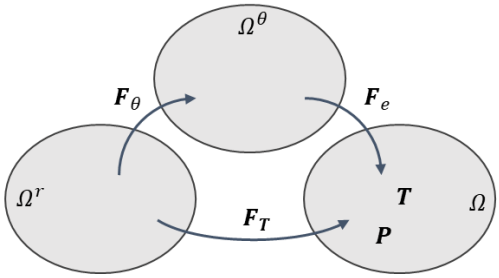

Figure 3. Transformation with the representation of the reference space, the fictitious intermediate configuration for thermal deformations and the current configuration.

Note that $\boldsymbol{F}_\theta$ and $\boldsymbol{F}_e$ link the transformations to a fictitious configuration Ω^θ representing an intermediate mapping through the reference Ω^r and the current Ω configurations. As discussed by Vujošević and Lubarda [12], $\boldsymbol{F}_e$ and $\boldsymbol{F}_\theta$ are in general local deformation gradients (two-point functions) and only $\boldsymbol{F}_T$ is a true deformation gradient for inhomogeneous deformations. The thermal deformation gradient for a given temperature variation $\Delta\theta = \theta_n - \theta_{ref}$ (in which the solid experiences a temperature θ_n above or below a stress-free reference temperature θ_{ref}) is

$$\mathbf{F}_\theta = (1 + \alpha\Delta\theta)\mathbf{I}, \tag{4}$$

where α is the coefficient of thermal expansion of the material. We assume the material is isotropic, and that its elastic behavior (due to its mechanical parameters) is independent from the thermal state and its evolution, resulting in an uncoupled thermoelastic formulation (the heat conduction problem is not considered here, such that the temperature field must be known a priori, i.e., given). The simplicity of this tensor due to the material´s isotropy allows us to describe the elastic part $\boldsymbol{F}_e$ explicitly as

$$\mathbf{F}_\mathrm{e} = \mathbf{F}_\mathrm{T}.\mathbf{F}_\theta^{-1} = (1 + \alpha\Delta\theta)^{-1}\mathbf{F}_\mathrm{T} = \beta\mathbf{F}_\mathrm{T}. \tag{5}$$

This description is important for a static formulation based on its energy-conjugate pair $\boldsymbol{P}$, which is the 1st Piola-Kirchhoff elastic stress tensor (in terms of its column-vectors, we write $\boldsymbol{P}$ as $\boldsymbol{P} = \boldsymbol{\tau}_{ei} \otimes \boldsymbol{e}_i$). The formulation starts from the equilibrium equations (and corresponding boundary conditions) described in the reference configuration by

$$\begin{cases} \operatorname{div} \mathbf{P} + \mathbf{b}^{\mathrm{r}} = \mathbf{0} & \text{in } \Omega^{\mathrm{r}} \\ \mathbf{u} = \bar{\mathbf{u}} & \text{in } \Gamma_{\mathrm{u}}^{\mathrm{r}} \\ \mathbf{t} = \bar{\mathbf{t}} & \text{in } \Gamma_{\mathrm{t}}^{\mathrm{r}} \end{cases} \tag{6}$$

where $\boldsymbol{b}^r$ is the vector of volume forces (per unit volume of the reference configuration) and $\boldsymbol{P}$ relates the traction vector $\boldsymbol{t}^r$ on a generic surface point (per unit area of the reference configuration) to its normal vector at the reference configuration $\boldsymbol{n}^r$, through $\boldsymbol{P}\boldsymbol{n}^r = \boldsymbol{t}^r$. The integral (weak) form of Eq. (6) is

$$\int_{\Omega^{\mathrm{r}}} \operatorname{div} \mathbf{P} \cdot \delta\mathbf{u} \mathrm{d}\Omega^{\mathrm{r}} + \int_{\Omega^{\mathrm{r}}} \mathbf{b}^{\mathrm{r}} \cdot \delta\mathbf{u} \mathrm{d}\Omega^{\mathrm{r}} = 0, \ \ \forall\, \delta\mathbf{u} \in \boldsymbol{\mathcal{V}}, \tag{7}$$

and, after invoking the divergence theorem and considering $\nabla \delta\boldsymbol{u} = \delta\boldsymbol{F}$ (satisfying Eq. (2)), one has

$$\int_{\Omega^{\mathrm{r}}} \mathbf{P} : \nabla\delta\mathbf{u} \mathrm{d}\Omega^{\mathrm{r}} = \int_{\Omega^{\mathrm{r}}} \mathbf{b}^{\mathrm{r}} \cdot \delta\mathbf{u} \mathrm{d}\Omega^{\mathrm{r}} + \int_{\Gamma^{\mathrm{r}}} \mathbf{t}^{\mathrm{r}} \cdot \delta\mathbf{u} \mathrm{d}\Omega^{\mathrm{r}}, \quad \forall\, \delta\mathbf{u} \in \boldsymbol{\mathcal{V}}, \tag{8}$$

where $\delta\boldsymbol{u}$ and $\delta\boldsymbol{F}$ are respectively the virtual displacement field and the virtual deformation gradient belonging to the subspace of weight functions $\boldsymbol{\mathcal{V}}$. The left side of the Eq. (8) is known as the internal virtual work δW_{int}, and can be represented in terms of the column-vectors of the integrands as

$$\delta \mathrm{W}_{\mathrm{int}} = \int_{\Omega^{\mathrm{r}}} \mathbf{P} : \delta\mathbf{F} \mathrm{d}\Omega^{\mathrm{r}} = \int_{\Omega^{\mathrm{r}}} \boldsymbol{\tau}_{\mathrm{ei}} \cdot \delta\boldsymbol{\gamma}_{\mathrm{ei}} \mathrm{d}\Omega^{\mathrm{r}} = \int_{\Omega^{\mathrm{r}}} \beta . \boldsymbol{\tau}_{\mathrm{ei}} \cdot \delta\boldsymbol{\gamma}_{\mathrm{Ti}} \mathrm{d}\Omega^{\mathrm{r}}, \tag{9}$$

wherein we recall that $\beta = (1 + \alpha\Delta\theta)^{-1}$ as defined in Eq. (5). This allows us to describe δW_{int} in terms of total virtual displacement gradient.

Considering that the objective is to obtain the displacement field $\boldsymbol{u}_T(x) \in \boldsymbol{\mathcal{S}}$ (subspace of approximation functions) that satisfies Eq. (8) $\forall\, \delta\boldsymbol{u} \in \boldsymbol{\mathcal{V}}$, and $\boldsymbol{u}_T(x)$ is the displacement associated by total transformations, the use of displacement gradient $\boldsymbol{\gamma}_{Ti}$ in the virtual term $\delta\boldsymbol{\gamma}_{Ti} = (1 + \alpha\Delta\theta).\delta\boldsymbol{\gamma}_{ei}$ (with the relation presented by the Eq. (5) and according to Eq. (2) expressions) allows us to represent the internal virtual work in the elastic part of the transformation based on the total displacement field $\boldsymbol{u}_T$. Within this approach, the virtual work principle (Eq. (8)) becomes

$$\int_{\Omega^{\mathrm{r}}} \beta . \boldsymbol{\tau}_{\mathrm{ei}} \cdot \delta\boldsymbol{\gamma}_{\mathrm{Ti}} \mathrm{d}\Omega^{\mathrm{r}} = \int_{\Omega^{\mathrm{r}}} \mathbf{b}^{\mathrm{r}} . \delta\mathbf{u} \mathrm{d}\Omega^{\mathrm{r}} + \int_{\Gamma^{\mathrm{r}}} \mathbf{t}^{\mathrm{r}} . \delta\mathbf{u} \mathrm{d}\Omega^{\mathrm{r}}, \quad \forall\, \delta\mathbf{u} \in \boldsymbol{\mathcal{V}}. \tag{10}$$

2.2 Hyperelastic constitutive equation

The so-called Simo-Ciarlet hyperelastic material law is used due to its simplicity to compute the elastic tangent stiffness matrix and also due to its good convergence behavior, compared with the classical (hyperelastic) Kirchhoff Saint-Venant law. This is justified by the poli-convexity of the strain energy function ψ, which guarantees the material stability and the existence of a strain state which minimizes the energy – condition for the existence of a solution (see Ciarlet [13] and Lahuerta [14]). The proposed strain energy density function is given by (Pimenta [15])

$$\psi(\mathrm{J}, \mathrm{I}) = \frac{\lambda}{2}\left[\frac{1}{2}(\mathrm{J}^2 - 1) - \ln(\mathrm{J})\right] + \frac{\mu}{2}(\mathrm{I} - 3 - 2\ln(\mathrm{J})) \tag{11}$$

with the invariants of $\boldsymbol{F}_e$, $J = \det(\boldsymbol{F}_e)$ and $I = \boldsymbol{f}_{ei} \cdot \boldsymbol{f}_{ei}$ related to the elastic strains; λ and μ are the Lamé coefficients. The column vector $\boldsymbol{\tau}_{ei}$ from 1st Piola-Kirchhoff stress tensor is given by the partial

derivative of ψ with respect to $\boldsymbol{\gamma}_{ei}$ or $\boldsymbol{f}_{ei}$ as

$$\boldsymbol{\tau}_{\mathrm{ei}} = \frac{\partial \psi}{\partial \boldsymbol{\gamma}_{\mathrm{ei}}} = \frac{\partial \psi}{\partial \mathbf{f}_{\mathrm{ei}}} = \frac{\partial \psi}{\partial \mathrm{J}} \frac{\partial \mathrm{J}}{\partial \mathbf{f}_{\mathrm{ei}}} + \frac{\partial \psi}{\partial \mathrm{I}} \frac{\partial \mathrm{I}}{\partial \mathbf{f}_{\mathrm{ei}}}. \tag{12}$$

Developing the expression above (see Gomes [10]) the vectors $\boldsymbol{\tau}_{ei}$ and $\boldsymbol{\tau}_{Ti}$ obtained are

$$\boldsymbol{\tau}_{\mathrm{ei}} = \left(\tfrac{\lambda}{2}(\mathrm{J}^2 - 1) - \mu\right)\mathrm{J}^{-1}\mathbf{g}_{\mathrm{ei}} + \mu \mathbf{f}_{\mathrm{ei}} \quad \text{and} \quad \boldsymbol{\tau}_{\mathrm{Ti}} = \beta^2 . \left(\left(\tfrac{\lambda}{2}(\mathrm{J}^2 - 1) - \mu\right)\mathrm{J}^{-1}\mathbf{g}_{\mathrm{Ti}} + \mu \mathbf{f}_{\mathrm{Ti}}\right), \tag{13}$$

with $\boldsymbol{g}_1 = -skew(\boldsymbol{e}_3)\boldsymbol{f}_2$ and $\boldsymbol{g}_2 = skew(\boldsymbol{e}_3)\boldsymbol{f}_1$. The terms for the fourth-order tensor of elastic tangent moduli for the pair $\{\boldsymbol{P}, \boldsymbol{F}\}$ can be found through the second-order components $\boldsymbol{C}_{ij}$.This tensor will provide the global tangent stiffness $\boldsymbol{K}_{Tg}$ to be numerically solved to obtain the displacement field that satisfies Eq. (8) at each time-step. As the Eq. (10) is related to the total displacement $\boldsymbol{u}_T$, the guarantee of quadratic convergence is dependent of the correct derivation based on Eq. (13) with respect to the total deformation gradient $\boldsymbol{f}_{Tj}$ to obtain a consistent $\boldsymbol{C}_{Tij}$. This one is calculated as

$$\mathbf{C}_{\mathrm{Tij}} = \frac{\partial \boldsymbol{\tau}_{\mathrm{Ti}}}{\partial \boldsymbol{\gamma}_{\mathrm{Tj}}} = \frac{\partial \boldsymbol{\tau}_{\mathrm{Ti}}}{\partial \mathbf{f}_{\mathrm{Tj}}} = \frac{\partial^2 \psi}{\partial \mathbf{f}_{\mathrm{Ti}} \partial \mathbf{f}_{\mathrm{Tj}}} =$$

$$= [\bar{\phi}(\mathrm{J})]\mathbf{g}_{\mathrm{i}} \otimes \mathbf{g}_{\mathrm{i}} + \beta^2 . \left[\delta_{\mathrm{ij}} . (\mu \mathbf{I} + \phi(\mathrm{J})\mathrm{skew}(\mathbf{e}_3)) - \phi(\mathrm{J})\mathrm{skew}(\mathbf{e}_3)\right] \tag{14}$$

in which δ_{ij} is de Kronecker's delta and the functions $\bar{\phi}(J)$ and $\phi(J)$ are (see Gomes [10])

$$\bar{\phi}(\mathrm{J}) = \tfrac{\lambda}{2}(1 + \mathrm{J}^{-2}) + \mu \mathrm{J}^{-2} \quad \text{and} \quad \phi(\mathrm{J}) = \left[\tfrac{\lambda}{2}(\mathrm{J}^2 - 1) - \mu\right]\mathrm{J}^{-1}. \tag{15}$$

Similarly to Eq. (12), the Cauchy stress tensor $\boldsymbol{T}$ is obtained as

$$\mathbf{T} = \mathrm{J}^{-1} \frac{\partial \psi}{\partial \mathbf{F_e}} . \mathbf{F}_{\mathrm{e}}^{\mathrm{T}} = \mathrm{J}^{-1} \mathbf{P} \mathbf{F}_{\mathrm{e}}^{\mathrm{T}}. \tag{16}$$

2.3 Consideration of damage effects

Applying the concepts of equilibrium and compatibility through the presented framework, it is important to impose the verification of the strain state in Ω region in order to evaluate the sufficiency of the material to support the applied traction. Within a simplified approach, Rabotnov (1968, apud Lemaitre [16]) presented this concept for one-dimensional monotonic load tests through the consideration of an effective stress $\tilde{\sigma}$ acting in an intact representative volume element (RVE) which represents an already damaged volume subjected to a true stress σ, $\sigma \leq \tilde{\sigma}$. This one is obtained by adopting a scalar parameter of damage density, d, obtained from the relation between the damaged and total areas of the real volume. Thus, it is obtained

$$\tilde{\sigma} = \sigma . (1 - \mathrm{d_n})^{-1}, \tag{17}$$

in which $d \in [0,1]$ is null for a undamaged region and 1 for a full damaged one. This relation can be extended to the loss of material stiffness through the reduction of the initial elasticity modulus E_0, considering an isotropic material within a two-dimensional problem, as

$$\tilde{\mathrm{E}}_{\mathrm{n}} = \mathrm{E}_0 . (1 - \mathrm{d_n}). \tag{18}$$

This is a very simple approach for a damage modelling, since more robust models also consider damage anisotropy with the evolution of a damage tensor (as presented by Murakami [17]), where the damage is relative to a reference base. Other approaches includes the damage evaluation under cyclic loads and unilateral conditions, in which the stiffness can be recovered due to crack closure (see Mazars [18] and Pijaudier-Cabot [19]) and coupled with plastic strains, as presented by Simo and Ju [20]. The scalar damage model proposed by Mazars [18, 21] seeks to represent the concrete brittle behavior,

presented in this paper, starting from the consideration of the Helmholtz free energy Ψ state potential through a formulation in the light of thermodynamics. With Ψ are evaluated the stresses and the variation of the internal elastic energy by the evolution of a damage strain energy release rate (Y) due to micro-cracks nucleation and voids growth. Considering the presented isotropic hyperelastic material characterized by $\psi(J, I)$ and its specific mass ρ_0,

$$\Psi = \widehat{\Psi}(\mathbf{F}_e, d) = \frac{1}{\rho_0}\widehat{\psi}(J, I, d) = \frac{1}{\rho_0}[(1-d)\psi(J, I)] \tag{19}$$

and the components of 1st Piola-Kirchhoff column vectors are written simply as

$$\boldsymbol{\tau}_{ei} = (1-d)\frac{\partial \psi}{\partial \boldsymbol{\gamma}_{ei}} = (1-d)\frac{\partial \psi}{\partial \mathbf{f}_{ei}}. \tag{20}$$

The energy release rate is obtained as the partial derivation of $\hat{\psi}$ with respect to damage evolution and

$$Y = \frac{\partial \widehat{\psi}}{\partial d} = -\psi(J, I). \tag{21}$$

The Clausius-Duhem inequality condition for the second thermodynamics law is verified if

$$Y\dot{d} \geq 0 \qquad \text{and} \qquad Y > 0 \;\rightarrow\; \dot{d} \geq 0, \tag{22}$$

which implies that the scalar damage evolution must be crescent throughout the thermoelastic process.

Mazars' classical damage model considers the initiation and growth of microcracks into concrete matrix being governed by a yield surface function $f(\tilde{\varepsilon}, \mathcal{K}_d)$ from strain space which delimits a limit region for a purely elastic behavior. This function is presented as

$$f(\tilde{\varepsilon}, \mathcal{K}_d) = \tilde{\varepsilon} - \mathcal{K}_d \leq 0, \tag{23}$$

where $\mathcal{K}_d$ is a damage-dependent parameter defined as the largest equivalent strain value in the whole time history, compared to an initial strain threshold value $\mathcal{K}_0$ from which the damage process starts. So,

$$\mathcal{K}_d = \widehat{\mathcal{K}}_d(d) = \max\{\mathcal{K}_0, \max_{t=[0,n]}(\tilde{\varepsilon})\}, \tag{24}$$

and the equivalent strain $\tilde{\varepsilon}$ is obtained from the positive part of the symmetric strain tensor as a projection of the strains associated to the positive eigenvalues (as defined by Simo and Ju [20]). In other words,

$$\tilde{\varepsilon} = \|\langle \varepsilon_i \rangle_+\| \quad \text{,with} \quad \langle \varepsilon_i \rangle_+ = (\varepsilon_i + |\varepsilon_i|)/2 \tag{25}$$

in which the Green-Lagrange tensor $\boldsymbol{E}$ is used to calculate the eigenvalues ε_i as the following

$$\varepsilon_i = \text{eig}(\mathbf{E})_i = \text{eig}\left(\tfrac{1}{2}\left(\mathbf{F}_e{}^T\mathbf{F}_e - \mathbf{I}\right)\right)_i. \tag{26}$$

Inside Mazars' model the damage evolution imposed to each element is related to two exponential laws which englobes tension (T) and compression (C) damages as a function of the equivalent strain $\tilde{\varepsilon}$ and the material parameters A_C, A_T, B_C and B_T (whose general ranges are indicated by Mazars and Pijaudier-Cabot, e.g. in [22]). Both functions for tension and compression presents the form

$$d_k = \hat{F}_k(\tilde{\varepsilon}) = 1 - [(1-A_k)\mathcal{K}_0/\tilde{\varepsilon}] - \left[A_k/\exp\left(B_k(\tilde{\varepsilon} - \mathcal{K}_0)\right)\right] \tag{27}$$

with $k = (T, C)$ and compose a total scalar damage value d thorough a composition dependent of scalar coefficients α_T and α_C (respecting $\alpha_T + \alpha_C = 1$). So $d = \alpha_T.d_T + \alpha_C.d_C$ and (see Álvares [23])

$$\alpha_k = {\varepsilon_{ki}^+}\Big/{\varepsilon_V^+} \quad \text{with} \quad \varepsilon_{ki}^+ = {(\varepsilon_{ki} + |\varepsilon_{ki}|)}\Big/{2} \quad \text{and} \quad \varepsilon_V^+ = (\varepsilon_{Ti}^+ + \varepsilon_{Ci}^+). \tag{28}$$

The components of strains ε_{Ci} and ε_{Ti} are stated from the partition of main stresses $\sigma_i = eig(\boldsymbol{P})_i$ as positive and negative parts, in which $\sigma_i^+ = \sigma_i + |\sigma_i|/2$ and $\sigma_i^- = \sigma_i - \sigma_i^+$. The positive stretching

strains ε_{ki}^{+} related to these main stresses were approached by the initial linear relation.

Remark 1: Concrete matrix, as other brittle materials, presents a rheological behavior in which damage tends to be significant after a tensile strain threshold (related to mode I in-plane crack opening). Due to this, the description of damage criterion through a parameter related to the total strain state of the solid proposed by Mazars is an interesting approach (especially considering the plane strain simplifications), besides the simplicity to compute this damage model. Another advantage is descripted in Simo and Ju [20] by the fact that damage mechanics is usually linked to the history of strains and not stresses (unlike habitual fracture mechanics criteria). For example, considering an unrestrained bar submitted to a heating process, is possible to observe crescent strains without any stress evolution (which is valid if a concrete matrix homogeneity simplification is adopted). This is expected as the bar is free to rearrange itself due to material dilatation. Based in the proposed thermoelastic formulation, in which is possible to observe total elastic and thermal tensile strains without necessarily tensile stresses, a stress driven damage model could leads to an incorrect response, at least without any stress result treatment before a damage evaluation (demanding additional calculation).

Remark 2: This damage model can only evaluate properly monotonic quasi-static load simulations without loading reversion. The damaged concrete response (represented by the stress-strain relation represented in Fig. 5) is inconsistent for cyclic or dynamic loads due to the existence of a single damage parameter that must respect entropy criteria. The stiffness lost by a specimen damaged under tensile strains is not recovered with the load inversion, e.g.. The representation of these behavior demands more robust formulation, as presented by la Borderie et al. [24] and other authors [19,25]. Owing to this modelling limitation, the proposed examples must regard only monotonic loading.

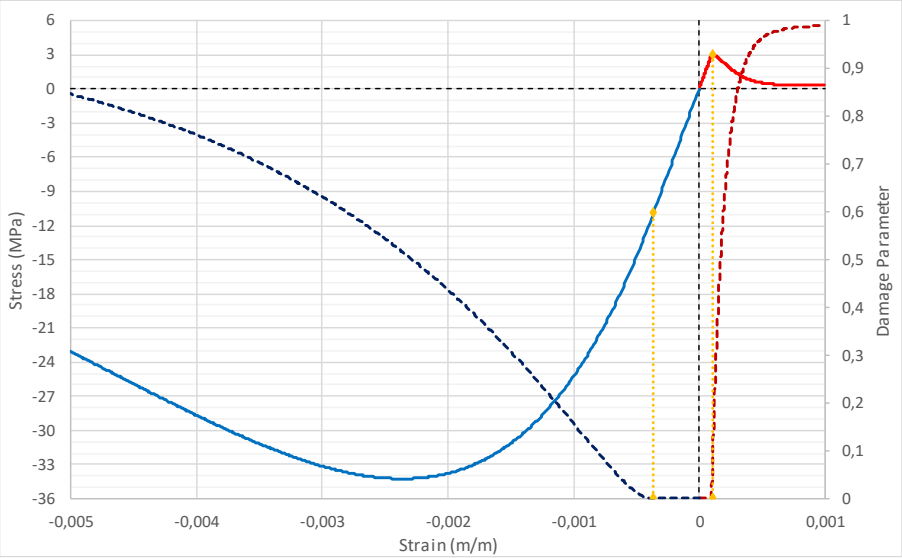

Figure 5. Mazar's model response for stress-strain and damage-strain curves of compression and tensile tests with usual damage parameters (as presented in Table 1).

2.4 FEM discretization

The framework method used to numerically solve the proposed structural problem is a standard Finite Element Method, in which the region Ω is discretized in Ne finite elements and the displacements field $\boldsymbol{u}(\boldsymbol{x})$ are approximated by polynomial shape functions, so

$$\mathbf{u}(\mathbf{x}) = \cup_{e=1}^{Ne} \mathbf{N}\mathbf{u}_\mathbf{e} \quad \textit{and} \quad \delta\mathbf{u}(\mathbf{x}) = \cup_{e=1}^{Ne} \mathbf{N}\delta\mathbf{u}_\mathbf{e}\,, \tag{29}$$

where $\mathbf{N}$ (the interpolation matrix) and $\mathbf{u_e}$ (the nodal displacements vector related to an element) are

given by

$$\mathbf{N} = [\mathrm{N}_1\mathbf{I}\ \mathrm{N}_2\mathbf{I}\ \ldots\ \mathrm{N}_\mathrm{n}\mathbf{I}] \quad \textit{and} \quad \mathbf{u_e} = [\mathrm{u}_1\ \mathrm{v}_1\ \mathrm{u}_2\ \mathrm{v}_2\ \ldots\ \mathrm{u}_\mathrm{n}\ \mathrm{v}_\mathrm{n}]^\mathbf{T} \tag{30}$$

for a problem wherein the element have n nodes and u and v are the displacement components (according to the orthonormal reference system base). The spatial derivation of $\mathbf{N}$ terms allows the approaching of the virtual displacement gradient $\delta\gamma_i$ as

$$\delta\gamma_\mathrm{i} = \mathbf{N}_{,\mathrm{i}}\delta\mathbf{u_e} = \left[\mathrm{N}_{1,\mathrm{i}}\mathbf{I}\ \mathrm{N}_{2,\mathrm{i}}\mathbf{I}\ \ldots\ \mathrm{N}_{\mathrm{n},\mathrm{i}}\mathbf{I}\right]\delta\mathbf{u_e}, \quad \textit{with} \quad \mathrm{i} = 1{,}2. \tag{31}$$

The application of Eq. (29) and Eq.(31) into the virtual internal work stated in Eq. (10) gives the internal and external force vectors $\mathbf{R}^e_{int}$ and $\mathbf{R}^e_{ext}$ of an element as

$$\delta\mathrm{W}^\mathrm{e}_\mathrm{int} = \int_{\Omega^\mathrm{r}_\mathrm{e}} \beta.\,\boldsymbol{\tau}_\mathrm{i}\cdot\delta\boldsymbol{\gamma}_{\mathrm{Ti}}\mathrm{d}\Omega^\mathrm{r}_\mathrm{e} = \delta\mathbf{u}^\mathrm{T}_\mathrm{e}\int_{\Omega^\mathrm{r}_\mathrm{e}} \beta.\,\mathbf{N}^\mathrm{T}_{,\mathrm{i}}\boldsymbol{\tau}_\mathrm{i}\,\mathrm{d}\Omega^\mathrm{r}_\mathrm{e} = \delta\mathbf{u}^\mathrm{T}_\mathrm{e}\mathbf{R}^\mathrm{e}_\mathrm{int} \tag{32a}$$

$$\delta\mathrm{W}^\mathrm{e}_\mathrm{ext} = \delta\mathbf{u}^\mathrm{T}_\mathrm{e}\left(\int_{\Omega^\mathrm{r}_\mathrm{e}}\mathbf{N}^\mathrm{T}\mathbf{b}^\mathrm{r}\mathrm{d}\Omega^\mathrm{r}_\mathrm{e} + \int_{\Gamma^\mathrm{r}_\mathrm{e}}\mathbf{N}^\mathrm{T}\mathbf{t}^\mathrm{r}\mathrm{d}\Gamma^\mathrm{r}_\mathrm{e}\right) = \delta\mathbf{u}^\mathrm{T}_\mathrm{e}\mathbf{R}^\mathrm{e}_\mathrm{ext}\,. \tag{32b}$$

As the objective is to obtain the global displacement field $\boldsymbol{r}$ that balances the internal and external virtual works, the problem reduces to a nonlinear relation dependent of $\boldsymbol{r}$ that must satisfies Eq.(32). With an assembly operator $\mathbf{A}_\mathrm{e}$ the unbalanced force vector $\mathbf{R}$ related to global dof components is

$$\begin{gathered}\mathbf{R}(\mathbf{r}) = \textstyle\sum_{\mathrm{e}=1}^{\mathrm{Nel}}\mathbf{A}^\mathrm{T}_\mathrm{e}\mathbf{R}^\mathrm{e}_\mathrm{int} - \sum_{\mathrm{e}=1}^{\mathrm{Nel}}\mathbf{A}^\mathrm{T}_\mathrm{e}\mathbf{R}^\mathrm{e}_\mathrm{ext} = \mathbf{R}_\mathrm{int}(\mathbf{r}) - \mathbf{R}_\mathrm{ext} = \mathbf{0}\ \ \forall\delta\mathbf{r}, \\ \textit{with}\ \ \delta\mathbf{r} = \textstyle\sum_{\mathrm{e}=1}^{\mathrm{Nel}}\mathbf{A}^\mathrm{T}_\mathrm{e}\,\delta\mathbf{u_e}.\end{gathered} \tag{33}$$

A standard Newton-Raphson solver is adopted in order to solve the nonlinear relation described by Eq. (33). This numerical method needs the calculation of the tangent stiffness matrix $\mathbf{K}_{Te}$ (calculated through de derivation of $\mathbf{R}^e_{int}$ by means of element total displacement $\mathbf{u_e}$) which is

$$\mathbf{K}_\mathrm{Te} = \int_{\Omega^\mathrm{r}_\mathrm{e}} \beta.\,\mathbf{N}^\mathrm{T}_{,\mathrm{i}}\mathbf{C}_{\mathrm{Tij}}\mathbf{N}_{,\mathrm{j}}\,\mathrm{d}\Omega^\mathrm{r}_\mathrm{e}\,. \tag{34}$$

3 Numerical examples

The authors implemented the proposed plane strain formulation in an in-house nonlinear FEM code and using GiD, a pre- and post-processor. The examples to be explored in this section provide a general understanding of the hyperelastic nonlinear problem and the damage evolution:

Example 1 – Slender simply supported-guided-in-x column subjected to thermal expansion;
Example 2 – Slender fixed-simply supported slab on an elastic foundation subjected to thermal expansion.

Table 1 presents a resume of geometrical and mechanical properties for each example, in which the damage parameters were defined considering Pijaudier-Cabot [22] limits recommendation. The models were discretized with 6 node triangular elements with a mesh refinement that limited the element to a maximum size of 20 mm for the most significant areas (areas in which the damage formation is significant). Figure 4 presents the mesh used for the examples and the boundary conditions adopted for each one. Considering the classic theory of plates and shells, both examples 1 and 2 present the linear Euler's buckling load $\mathrm{P_{cr}}$ dependent of effective flexural stiffness $EI/(1-\nu^2)$ and the effective height

l_e as

$$P_{cr} = \frac{\pi^2 EI}{(1-\nu^2)\, l_e{}^2}. \tag{34}$$

From Eq. (34), the equivalent linear Euler's buckling temperature variation $\Delta\theta_{cr}$ for an exclusively thermal problem can be evaluated as

$$\Delta\theta_{cr} = \frac{\pi^2\, I}{\alpha A(1-\nu^2) l_e{}^2} \tag{35}$$

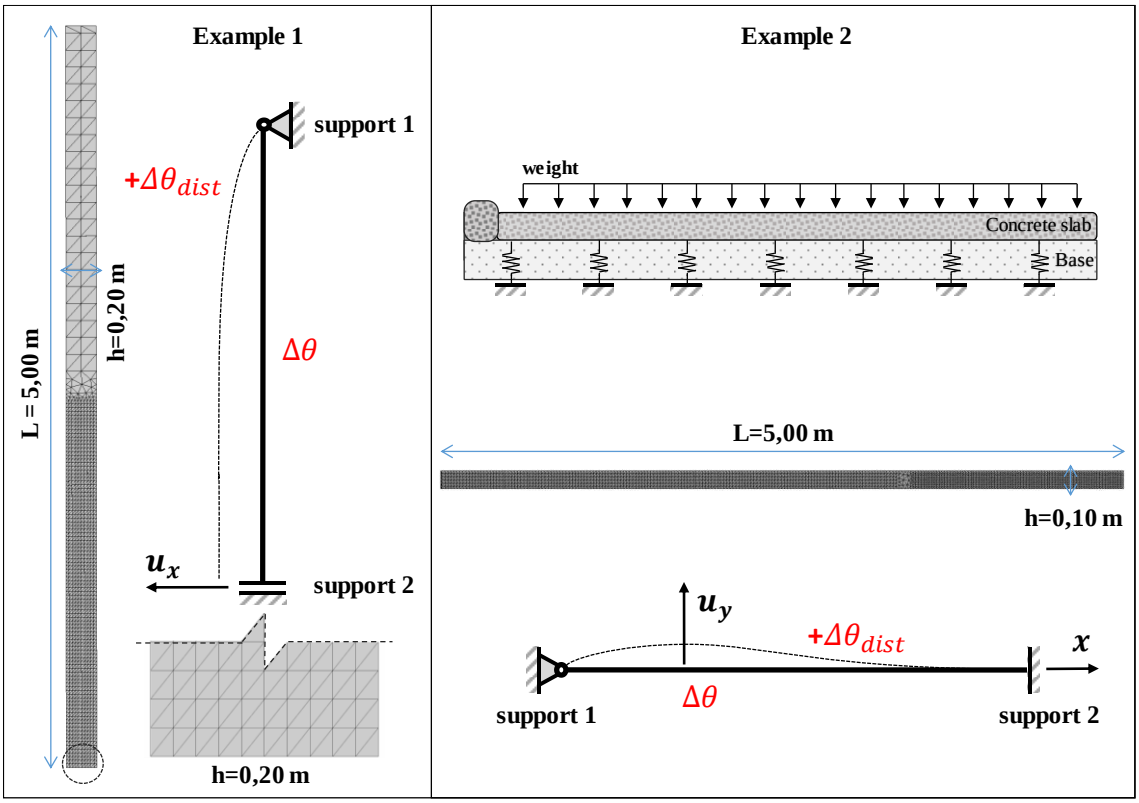

Figure 4. Boundary conditions and mesh used for each example

Table 1. General mechanical and geometrical properties.

	Example 1	**Example 2**
- Mechanical Properties -	*Concrete*	*Concrete*
Self weight W (N/m^3)	24,0e+3	24,0e+3
Young's Modulus E (N/m^2)	3,00e+10	3,00e+10
Poisson's ratio ν	0,20	0,20
Thermal expansion coefficient. α ($°C^{-1}$)	1,00e-5	1,00e-5
- Geometrical Properties-	*Column*	*Pavement*
Model Lenght L (m)	5,00	6,00
Model height h (m)	0,20	0,15
Effective Lenght l_e (m)	10,00	4,20
Model thickness t (m)	1,00	1,00

- Damage Properties -	A_T	B_T	A_C	B_C	$\mathcal{K}_0$
	0,90	1,00e+4	1,20	1,50e+3	3,00e-4

Example 1 neglects the column self-weight as load input. Instead of it, example 2 considers a vertical distributed load of 2400 N/m equivalent to the pavement concrete slab self-weight. The elastic foundation reacts only in cases where u_y is negative, that is, in cases of soil/base compression. Otherwise, the elastic foundation stiffness contribution should be null, resulting in a discontinuous response. The distributed stiffness applied to this case was evaluated through a comparison with concrete's elastic modulus and the value adopted is in order of 10^{15} N/m.

3.1 Example 1 - Column subjected to thermal expansion

Figure 5 presents the support 2 horizontal displacement u_x for the example 1. For this case the displacement evolution is related to the increment of temperature $\Delta\theta$ and the vertical axis indicates these values normalized by the critical load P_{cr} or temperature $\Delta\theta_{cr}$, as presented in Eq. (35). Each curve was subjected to a different initial disturbance temperature gradient $\Delta\theta_{dist}$ which remains constant along the increase of $\Delta\theta$. The application of a linear temperature gradient along the section width (0.20 m) allows to observe an initial constant curvature in the column. The increase of this initial gradient $\Delta\theta$ moves away the column behaviour from the bifurcation point and turns the flexural behaviour more significant than compression. The dashed black line represent reference undamaged paths with the minimum initial temperature variation to avoid disturbing the pre- and post-buckling response.

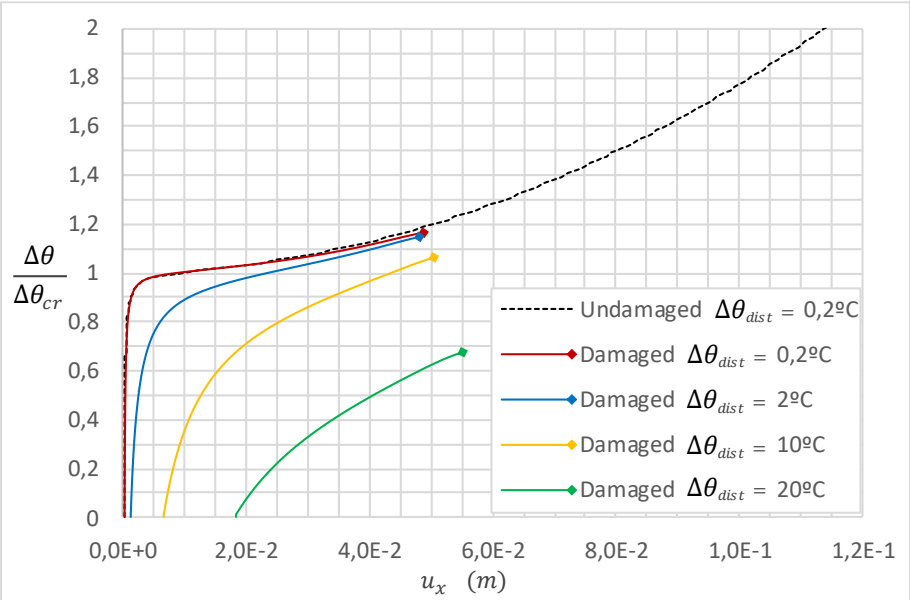

Figure 5. Variation of horizontal displacement with the increase of temperature $\boldsymbol{\Delta\theta}$.

The results in Fig. 5 also indicate the endpoint for each case in which the existent damage takes the concrete section to ruin, considering each initial temperature gradient. As seen in Fig. 5, final temperature ratio is smaller for higher initial temperature gradients. Fig. 6 presents the horizontal displacement u_x and the damage at the endpoint (presented in Fig. 4). These "pictures" indicate that the damage state for all the initial $\Delta\theta_{dist}$ ($0.2\,ºC$, $2\,ºC$, $10\,ºC$ and $20\,ºC$) were similar at the endpoints, despite the final temperature differences.

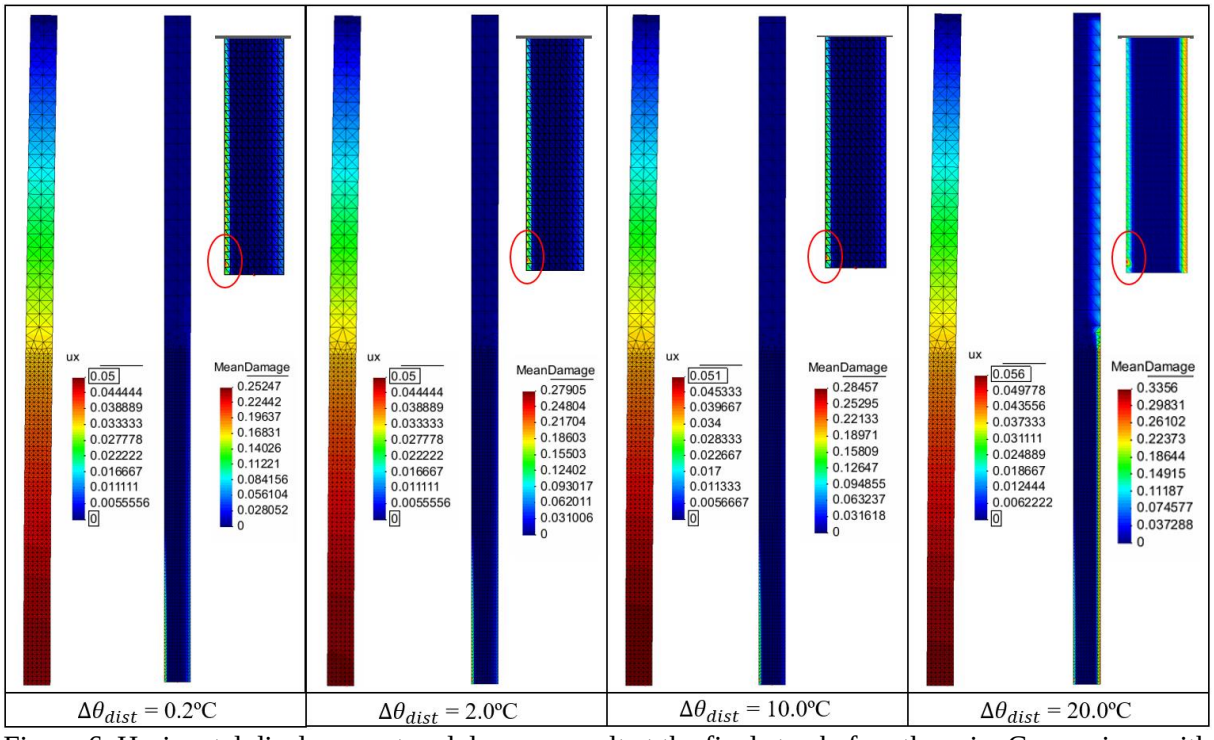

Figure 6. Horizontal displacement and damage result at the final step before the ruin. Comparison with the increase of initial disturbance temperature $\boldsymbol{\Delta\theta_{dist}}$.

The Fig. 7 and the Fig. 8 present the damage (d) and the Cauchy vertical stress ($\sigma_y = T_{22}$) evolution for each curve presented in Fig. 5, respectively. This values were captured in the column's support 2, where Fig. 6 indicated the most significant damages and displacements profiles. Figure 8 particularly

helps to understand the damage initiation based in the stress evolution. The abrupt behavior change from uniform compression to flexo-compression (eccentric) at support 2 section is due to the post-buckling effect, mainly for the cases with small disturbance temperature. The cases with $\Delta\theta_{dist} = 10ºC$ or $20ºC$ already present from the beginning an initial significant flexed section and the evolution from compressive to flexural behavior is smoother, while the damage occurs end evolves at more primary stages. This result demonstrates the initial disturbance role (be it geometric or load-originated) not only in the column displacement response (fitting or not with the pre- and post-buckling paths) but also in the structural capacity to withstand the load pattern imposed by that one.

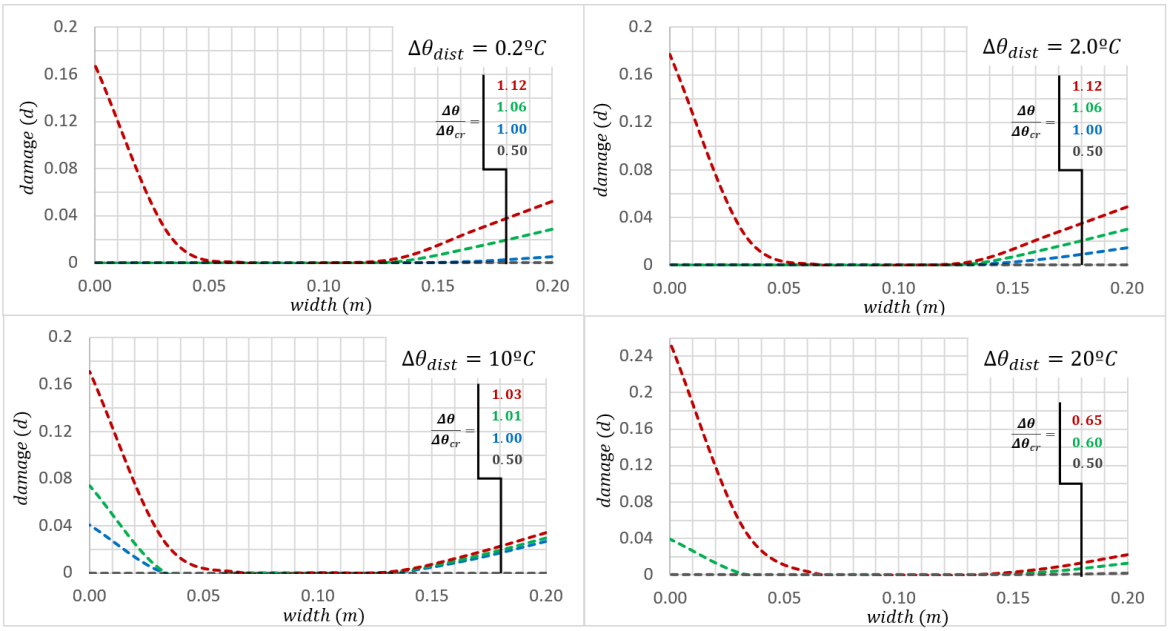

Figure 7. Support 2 damage contour at some steps of temperature (as indicated).

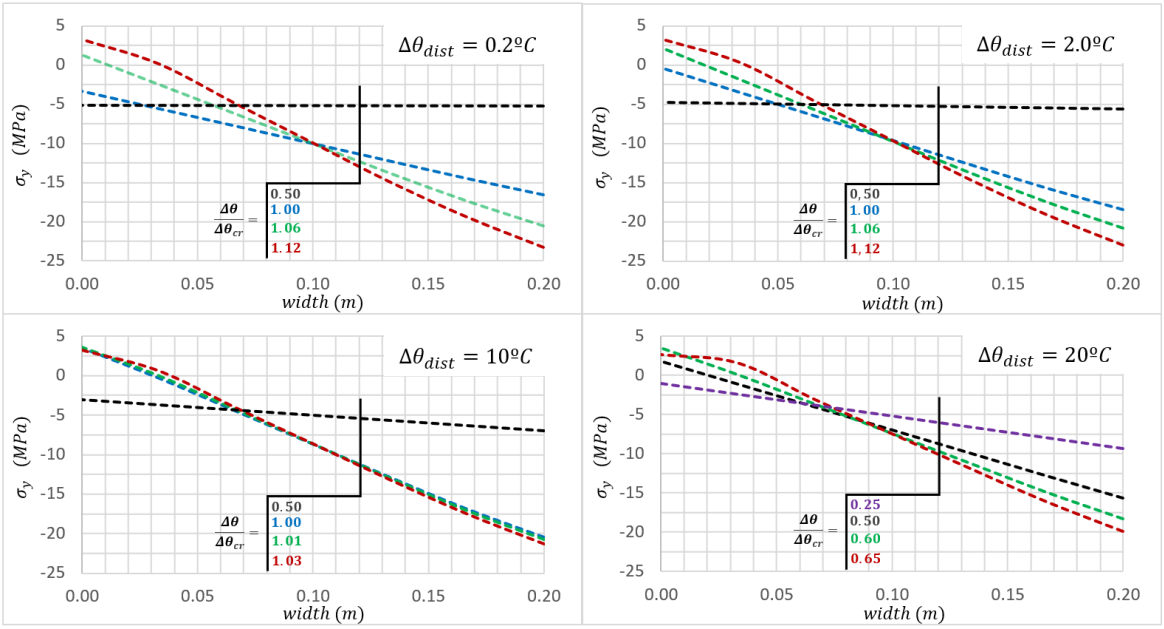

Figure 8. Support 2 vertical stress ($\boldsymbol{\sigma_y - MPa}$) contour at some steps of temperature (as indicated).

3.2 Example 2 - Slab on an elastic foundation

Figure 9 presents the maximum vertical displacement u_y for example 2 (where the black curve was kept from example 1 as a reference.). Green curve considers example 2 boundary conditions without self-weight and the elastic foundations and captures the buckling effect with the positive variation of temperature ($\Delta\theta$). Red curve do consider the elastic foundation and the concrete self-weight. Both consider the same disturbance initial temperature of 1.5 ºC. Figure 10 present the damage for the solution with elastic foundation. Comparing undamaged solutions with and without weight and elastic foundation inclusion, the different way the vertical displacement field evolves along the pavement slab heating is observable and is presented in Fig. 11. The positive vertical displacement is not mobilized by the whole pavement for small thermal variations (in which the self-weight still relevant and the foundation acts to balance both thermal and weight loads – see Fig. 12). Observe that support 1 is free to rotate and the pavement detachment from the rigid base starts there. The vertical displacement u_y (x) evolution is presented in Fig. 12 for the slab's middle section ($y = 0.05\ m$).

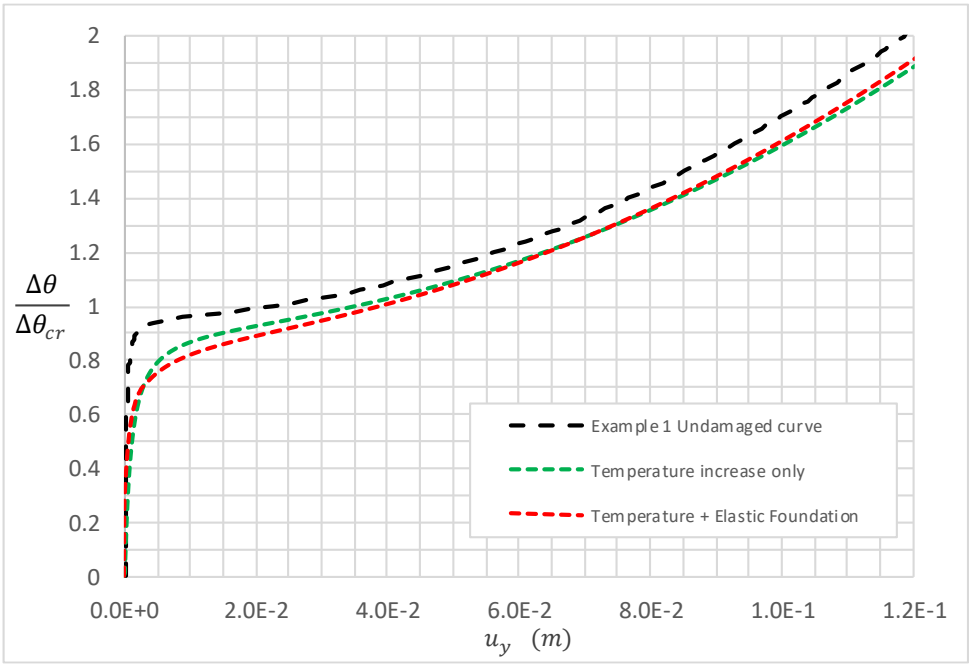

Figure 9. Maximum vertical displacement for example 2 cases with modifications.

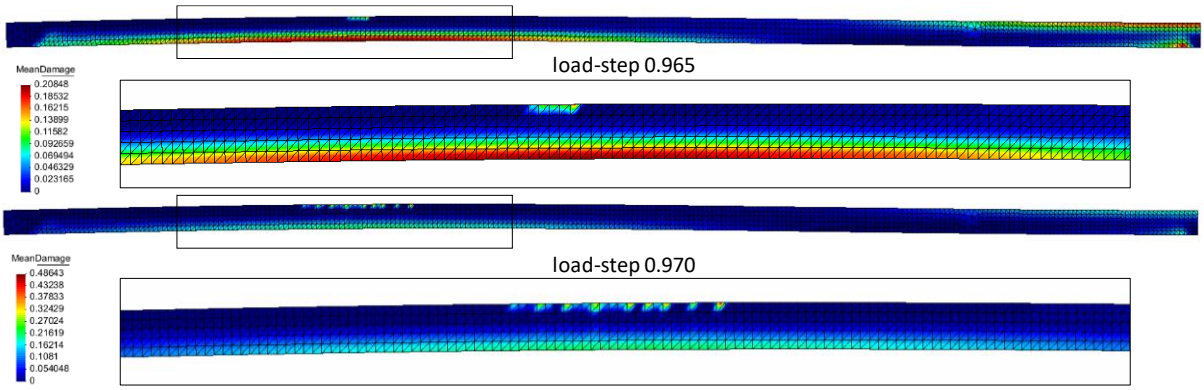

Figure 10. Damage evolution in load-steps 0.965 and 0.97 (last time-steps converged).

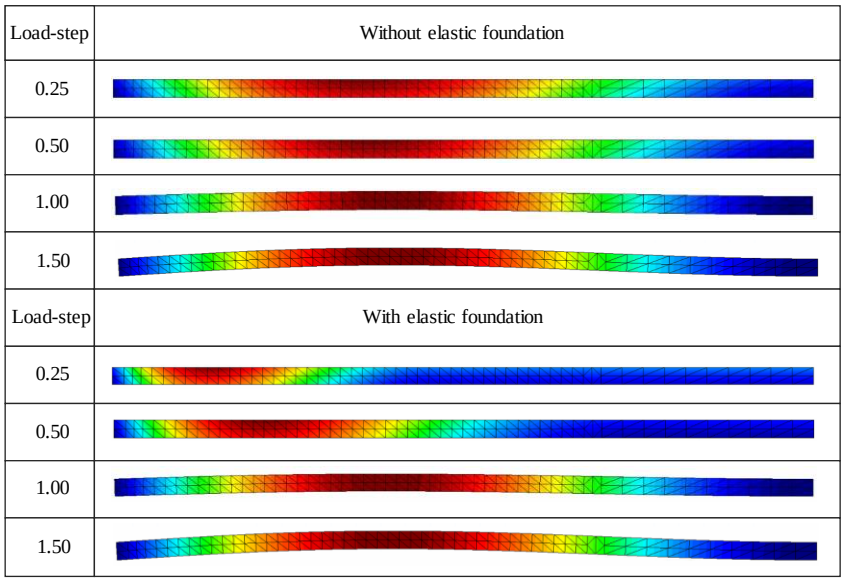

Figure 11. Vertical displacement comparison for Example 2 variations.

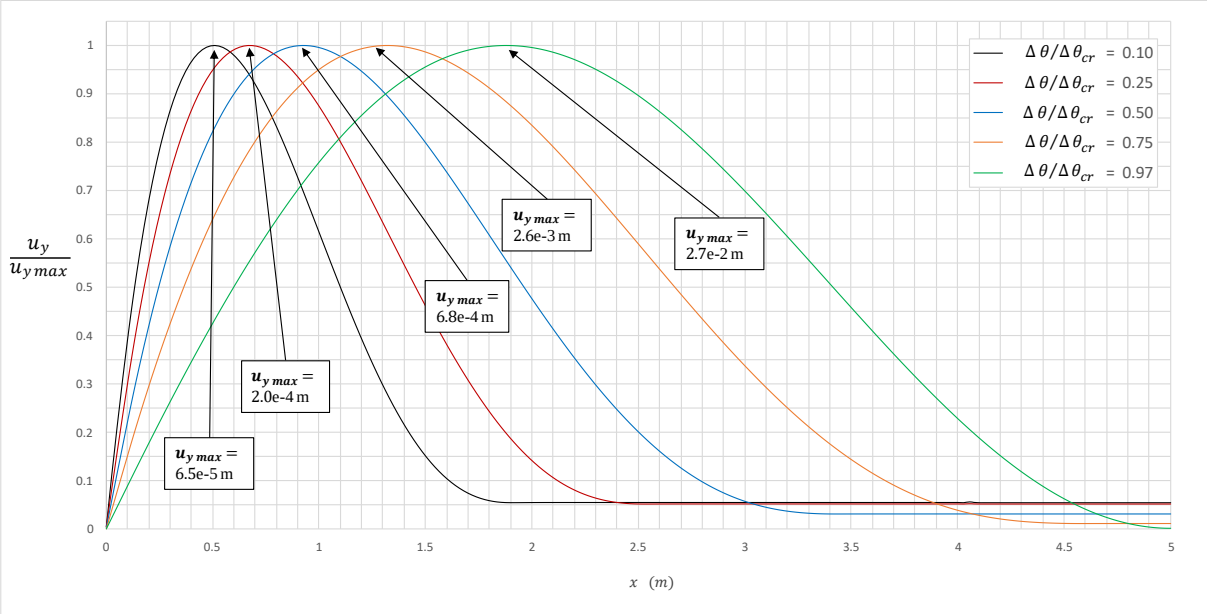

Figure 12. Dimensionless relative vertical displacement $\boldsymbol{u_y/u_{y\,max}}$ for Example 2 load-steps 0.1, 0.25, 0.5, 0.75 and ultimate 0.97 (last time-step converged).

4 Conclusions

The examples presented a general understanding of the stability problem related to bucking phenomenon within two different applications. Both problems demanded a consistent nonlinear thermoelasticity formulation due to the nature of the proposed external solicitations. The damaged zones growth was observed in the contour regions of the column/pavement, wherein more expressive tensile or compressive strains showed up. These solutions also presented a smoother evolution of damaged

related to compressive zones.

As can be seen in Fig. 6, 7 and 12, the ultimate load-step before numerical solution divergence presented a sudden evolution of tensile damage, which the authors assume to be an indicative of the cracking advance until the cross-section rupture. The standard Newton-Raphson method used in our FEM code is a responsible for this limitation. The use of advanced numerical solver methods (with displacement control or the Arc length's method) could lead us to results with a more expressive evolution in the damage field. Despite this, is important to consider that the damage growth phenomena was well-represented with the proposed solution, presenting a consistent stress-strain evolution for both examples.

Acknowledgements

First, third and fourth authors acknowledge fellowship funding from ANFACER (Brazilian Association of Manufactureres of Ceramic Tiles, Sanitary Ware and Related Products). Second author acknowledges support by CNPq (Conselho Nacional de Desenvolvimento Científico e Tecnológico), Brazil, under the grants 309748/2015-1 and 307368/2018-1.

References

[1] K. J. Elwood. Performance of concrete buildings in the 22 February 2011 Christchurch earthquake and implications for Canadian codes. *Canadian Journal of Civil Engineering*, vol. 40, pp. 759–776, 2013.

[2] Y. Bouras and Z. Vrcelj. Non-linear in-plane buckling of shallow concrete arches subjected to combined mechanical and thermal loading. *Engineering Structures*, vol. 152, n. 1, pp. 413–423, 2017.

[3] M.A. Vaz, J.C.R. Cyrino and A.C. Neves. Initial thermo-mechanical post-buckling of beams with temperature-dependent physical properties. *International Journal of Non-Linear Mechanics*, vol. 45, pp. 256-262, 2010.

[4] U. Bajc, M. Saje, I. Planinc and S. Bratina. Semi-analytical buckling analysis of reinforced concrete columns exposed to fire. *Fire Safety Journal*, vol. 71, pp. 110–122, 2015.

[5] B. Lai, J. Y. R. Liew and T. Wang. Buckling behaviour of high strength concrete encased steel composite columns. *Journal of Constructional Steel Research*, vol. 154, pp. 27–42, 2019.

[6] A. D. Kerr and P. J. Shade. Analysis of concrete pavement blowups. *Acta Mechanica*, vol. 52, pp. 201–224, 1984.

[7] G. Yang, M. A. Bradford. Thermal-induced upheaval buckling of concrete pavements incorporating the effects of temperature gradient. *Engineering Structures*, vol. 164, pp. 316–324, 2018.

[8] E. M. B. Campello. Modelos não-lineares de casca em elasticidade e elastoplasticidade com grandes deformações: teoria e implementação em elementos finitos [tese]. São Paulo: Escola Politécnica, 2005.

[9] E. M. B. Campello; P. M. Pimenta; P. Wriggers. A triangular finite shell element based on a fully nonlinear shell formulation. Computational Mechanics, Heidelberg, v. 31, n.6, pp. 505-518, 2003.

[10] H. C. Gomes. Método dos elementos finitos com fronteiras imersas aplicado a problemas de dinâmica dos fluidos e interação fluido-estrutura [tese]. São Paulo: Escola Politécnica, 2013.

[11] E. M. B. Campello; P. M. Pimenta; P. Wriggers. Elastic-plastic analysis of metallic shells at finite strains. Revista da Escola de Minas, v. 60, p. 381-389, 2007.

[12] L. Vujošević and V. A. Lubarda. Finite-strain thermoelasticity based on multiplicative decomposition of deformation gradient. *Theoretical and Applied Mechanics*, vol. 28-29, pp. 379–399, 2002.

[13] P. G. Ciarlet. *Mathematical Elasticity*. *Volume I: Three-Dimensional Elasticity*. Elsevier Science Ltd, 1988.

[14] R. D. Lahuerta. Projeto de mecanismos flexíveis baseado no efeito da flambagem não linear utilizando o método de otimização topológica [tese]. São Paulo: Escola Politécnica, 2017.

[15] P. M. Pimenta. *Fundamentos da Mecânica dos Sólidos e das Estruturas. Apostila do curso de Fundamentos I. Escola Politécnica da USP*. São Paulo, 2008.
[16] J. Lemaitre. *A Course on Damage Mechanics*. Springer, 1996.
[17] S. Murakami, K. Kamiya. Constitutive and damage evolution equations of elastic-brittle materials based on irreversible thermodynamics. *International Journal of Mechanical Sciences,* vol. 39, pp. 473-486, 1997.
[18] J. Mazars, G. Pijaudier-Cabot. Continuum Damage Theory - Application to Concrete. *Journal of Engineering Mechanics,* vol. 115, pp. 345-365, 1989.
[19] G. Pijaudier-Cabot, L. Jason. Continuum damage modelling and some computational issues. *Revue Française de Génie Civil*, vol. 6, pp. 991-1017, 2002.
[20] J. C. Simo, J. W. Ju. Strain- and stress-based continuum damage models - I. Formulation. International Journal of Solids and Structures, vol.23, pp.821-840, 1987.
[21] J. Mazars. A description of micro- and macroscale damage of concrete structures. *Engineering Fracture Mechanics*, vol. 25, pp. 729-737, 1986.
[22] G. Pijaudier-Cabot, J. Mazars. Damage models for concrete. *Jean Lemaitre Handbook of Materials Behavior Models.* Elsevier, pp. 500-512, 2001.
[23] M. S. Álvares. Estudo de um modelo de dano para o concreto: formulação, identificação paramétrica e aplicação com o emprego do método dos elementos finitos [tese]. São Carlos, EESC-USP, 1993.
[24] C. la Borderie, J. Mazars, G. Pijaudier-Cabot. Damage mechanics model for reinforced concrete structures under cyclic loading. *ACI Journal*, vol. 134, pp. 147-172, 1994.
[25] J. Mazars, Y. Berthaud, S. Ramtani. The unilateral behaviour of damaged concrete. *Engineering Fracture Mechanics*, vol. 35, pp.629-635, 1990.